

This document is confidential and is proprietary to the American Chemical Society and its authors. Do not copy or disclose without written permission. If you have received this item in error, notify the sender and delete all copies.

Emergent Ferromagnetism in CaRuO₃/CaMnO₃ (111)-oriented Superlattices

Journal:	<i>Nano Letters</i>
Manuscript ID	nl-2023-04623j.R3
Manuscript Type:	Communication
Date Submitted by the Author:	06-Feb-2024
Complete List of Authors:	Kane, Margaret; Stanford University, Materials Science and Engineering and Geballe Laboratory for Advanced Materials Bhandari, Churna; Ames Laboratory Holtz, Megan; Colorado School of Mines, Metallurgical and Materials Engineering Balakrishnan, Purnima; NIST Center for Neutron Research, Grutter, Alexander; National Institute of Standards and Technology, NIST Center for Neutron Research Fitzsimmons, Michael; Oak Ridge National Laboratory, Neutron Scattering Division Yang, Chao-Yao; National Yang Ming Chiao Tung University, Material Science and Engineering Satpathy, Sashi; University of Missouri, Physics and Astronomy Paudyal, Durga; Ames Laboratory, Division of Material Sciences and Engineering; Iowa State University, Electrical and Computer Engineering Suzuki, Yuri; Stanford University, Applied Physics and Geballe Laboratory for Advanced Materials

SCHOLARONE™
Manuscripts

Emergent ferromagnetism in $\text{CaRuO}_3/\text{CaMnO}_3$ (111)-oriented superlattices

Margaret Kane,^{*,†,△} Churna Bhandari,^{*,‡} Megan E. Holtz,[¶] Purnima P.
Balakrishnan,[§] Alexander J. Grutter,[§] Michael Fitzsimmons,^{||} Chao-Yao Yang,[⊥]
Sashi Satpathy,[#] Durga Paudyal,^{‡,∇} and Yuri Suzuki^{*,@,△}

[†]*Department of Materials Science and Engineering, Stanford University, Stanford, CA
94305, USA*

[‡]*Ames National Laboratory, Iowa State University, Ames, IA 50011, USA*

[¶]*Metallurgical and Materials Engineering, Colorado School of Mines, Golden, CO 80401,
USA*

[§]*NIST Center for Neutron Research, National Institute of Standards and Technology,
Gaithersburg, MD 20899, USA*

^{||}*Neutron Scattering Division, Oak Ridge National Laboratory, Oak Ridge, TN 37830 USA*

[⊥]*Department of Material Science and Engineering, National Yang Ming Chiao Tung
University, Hsinchu City 30100, Taiwan*

[#]*Department of Physics & Astronomy, University of Missouri, Columbia, Missouri 65211,
USA*

[@]*Department of Applied Physics, Stanford University, Stanford, CA 94305, USA*

[△]*Geballe Laboratory for Advanced Materials, Stanford University, Stanford, CA 94305,
USA*

[∇]*Department of Electrical and Computer Engineering, Iowa State University, Ames, Iowa
50011, USA*

E-mail: mmkane@stanford.edu; cbb@ameslab.gov; ysuzuki1@stanford.edu

Abstract

The boundary between CaRuO_3 and CaMnO_3 is an ideal testbed for emergent magnetic ground states stabilized through interfacial electron interactions. In this system, nominally antiferromagnetic and paramagnetic materials combine to yield interfacial ferromagnetism in the CaMnO_3 due to electron leakage across the interface. In this work, we show that the crystal symmetry at the surface is a critical factor determining the nature of the interfacial interactions. Specifically, by growing $\text{CaRuO}_3/\text{CaMnO}_3$ heterostructures along the (111) instead of (001) crystallographic axis, we achieve a threefold enhancement of the magnetization and involve the CaRuO_3 layers in the ferromagnetism, which now spans both constituent materials. The stabilization of a net magnetic moment in CaRuO_3 through strain effects is long-sought but never consistently achieved, and our observations demonstrate the importance of interface engineering in the development of new functional heterostructures.

Keywords

emergent magnetism, complex oxides, superlattices, ruthenates, manganites

Low dimensional ferromagnetism is of fundamental and technological interest, as the isolation of a net moment to the interface of a nonmagnetic material presents opportunities for fundamental spin transport and novel spin-based device studies.¹⁻⁶ The emergent interfacial ferromagnetism in (001)-oriented $\text{CaRuO}_3/\text{CaMnO}_3$ (CRO/CMO) superlattices is attributed to leakage of itinerant electrons from the metallic CRO into the insulating antiferromagnetic CMO layer, acting as a fractional charge transfer to Mn ions.⁷⁻¹³ Theoretical studies¹² and electron energy loss spectroscopy (EELS)⁹ indicate that these itinerant electrons stabilize a weak double exchange interaction among the interfacial Mn atoms of the CMO. The charge transfer magnitude decays rapidly away from the interface so that the ferromagnetic signal is isolated to the first unit cell of the CMO, where competition between superexchange and double exchange results in a canted moment of $0.85 \mu_B/\text{Mn} - 1.0 \mu_B/\text{Mn}$.

1
2
3 This emergent magnetic ground state can be tuned by applying an electric field, modu-
4 lating the double exchange to enable the suppression or full alignment of the surface Mn⁴⁺
5 ions for a maximum interfacial moment of 2.5 μ_B /Mn – 3.0 μ_B /Mn.¹¹ Alternatively, interfa-
6 cial structural symmetry can modify the interfacial magnetic moments of (001) CRO/CMO
7 and the closely related (001) LNO/CMO system.^{10,14} Specifically, changes in the tilt and
8 rotation pattern of the oxygen octahedra across the interface have yielded twofold vari-
9 ations in the interfacial magnetization.^{9,10} These observations suggest that changing the
10 crystallographic growth axis could yield dramatic changes in the magnetic ground state. In
11 fact, it has been previously demonstrated in heterostructures such as LaFeO₃/(La,Sr)MnO₃
12 that (111)-oriented interfaces can enhance the interlayer coupling, yielding a larger emergent
13 magnetization and modifying the antiferromagnetic spin textures.¹⁵ These observations have
14 been attributed to the change in symmetry and greater degree of octahedral connectivity
15 across the interface.¹⁶

16
17
18
19
20
21
22
23
24
25
26
27
28
29 The realization of CRO/CMO superlattices in the (111) direction offers a unique opportu-
30 nity to exploit the interplay between charge transfer and octahedral connectivity to stabilize
31 novel emergent magnetic ground states at atomically precise interfaces. Specifically, we ex-
32 pect modified orbital hybridization and, consequently, modified exchange interactions at the
33 interfaces. Further, the G-type antiferromagnetic order of CMO manifests ferromagnetically
34 aligned Mn moments along the (111) planes,¹⁷ which is likely to enhance the magnitude of
35 the emergent magnetism. Lastly, the (111) interfaces drive unique strain symmetries that
36 could stabilize altered magnetism and unique spin textures. Therefore the (111) orientation
37 may give rise to even more exotic emergent long range magnetic order.

38
39
40
41
42
43
44
45
46
47 In this letter, we examine a series of [(CaRuO₃)_N/(CaMnO₃)_M]₅ superlattices (SLs)
48 grown on (111) LaAlO₃ substrates by pulsed laser deposition (see methods in the Supple-
49 mental Materials). Thicknesses were varied for both CRO ($N = 6$ u.c. – 15 u.c.) and CMO
50 ($M = 3$ u.c. – 8 u.c.), where we define 1 u.c. (unit cell) as the distance between adja-
51 cent (111) planes, $d_{111}=0.223\text{nm}$. We demonstrate a novel emergent ferromagnetic ground
52
53
54
55
56
57
58
59
60

1
2
3 state arising from the interplay of interfacial charge transfer and interfacial strain symmetry
4 driven distortions. Surprisingly, the large resultant ferromagnetic moment appears to orig-
5 inate from both Mn and Ru ions, and the net magnetization is not exclusively confined to
6 the first unit cell as in the (001) orientation. This picture of the magnetism is supported
7 by *ab initio* calculations and structural and magnetic depth profiles extracted using polar-
8 ized neutron reflectometry. The enhanced Curie temperature of 175 K, compared to 100
9 K observed in the (001)-oriented system, points to stronger exchange interactions in the
10 (111) system. Scanning transmission electron microscopy (STEM) measurements and x-ray
11 reflectivity (XRR) reveal sharp interfaces. Together the magnetic and structural evidence
12 points to a new materials phase space for low dimensional ferromagnetism driven by charge
13 transfer and strain symmetry.

14
15 All SLs exhibited smooth surface morphology, and XRR measurements (supplemental
16 Figure S1) confirmed the low roughness and intended layer structure of the CRO/CMO
17 superlattices. Specifically, the interfacial and surface roughnesses were found to be below
18 0.7 nm for all samples, independent of measured net magnetism. We note that XRR mea-
19 surements include contributions from long-range thickness variations, conformal roughness
20 and intermixing across tens of microns, so that roughnesses extracted by fitting XRR data
21 represent an upper bound. Correspondingly, RMS roughnesses measured by $1 \mu\text{m} \times 1 \mu\text{m}$
22 AFM scans were lower and ranged from 0.24 nm to 0.66 nm. Both AFM and XRR mea-
23 surements are comparable to those measured from (001)-oriented SLs previously, and the
24 sub-nm roughnesses observed demonstrate high-quality interfaces in our (111)-oriented SLs.
25 Critically, the roughness remained fairly constant with increasing film thickness, indicating
26 that an increase in intermixing as layer thickness increases was unlikely.

27
28 For a more local examination of interface quality, we performed scanning transmission
29 electron microscopy (STEM). STEM scans of a $[(\text{CMO})_3/(\text{CRO})_{15}]_5$ superlattice confirm high
30 quality interfaces and distinct layers in our superlattices. As seen in Figure S2, the CMO
31 layer thickness shows some variation from 2 u.c. – 4 u.c., possibly due to the roughness of
32
33
34
35
36
37
38
39
40
41
42
43
44
45
46
47
48
49
50
51
52
53
54
55
56
57
58
59
60

the LaAlO_3 substrate or deposition of incomplete layers. This measurement supports the XRR data that indicate high quality (111) superlattices.

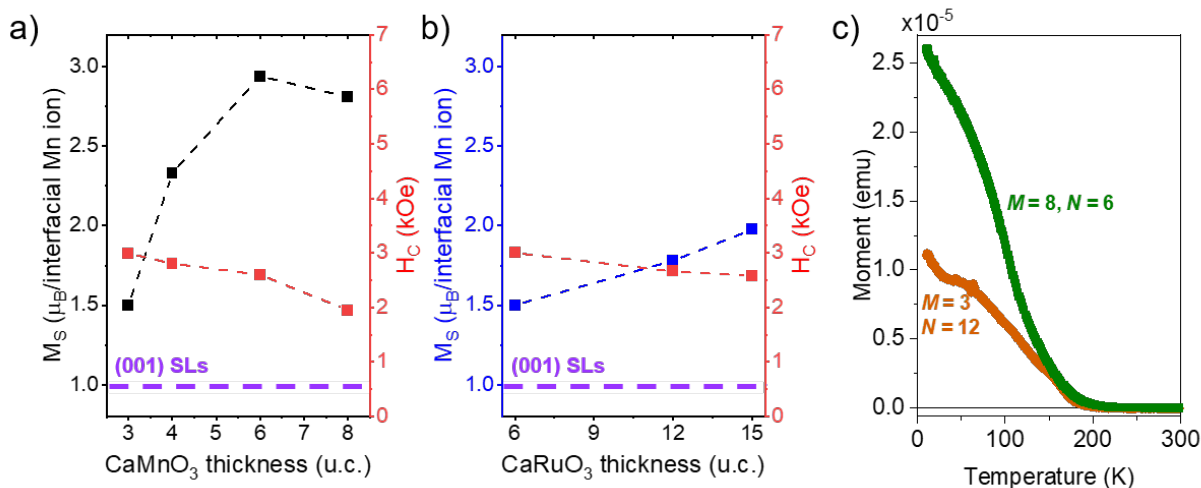


Figure 1: SQUID magnetometry measurements of CMO/CRO(111) superlattices (SLs), saturated moment of SLs a) varying CMO thickness (3 – 8 u.c.) and constant CRO thickness of 6 u.c., b) varying CRO thickness (6 – 15 u.c.) and constant CMO thickness of 3 u.c., c) magnetization with temperature for $[CMO_M/CRO_N]$ superlattices, field cooled at $H = 5$ T, measurement taken at $H = 5$ mT. $1 \text{ emu} = 1 \text{ mA}\cdot\text{m}^2$

SQUID magnetometry from (111) CRO/CMO SLs with varying CRO and CMO thicknesses revealed ferromagnetism in all samples but with larger moments than the (001)-oriented system. Further, we observed an unexpected thickness dependence of the saturation magnetization M_S . Specifically, M_S increased with both CRO and CMO thicknesses, as shown in Figure 1a,b. At a constant CRO thickness of $N = 6$ u.c., increasing CMO thickness from $M = 3 - 8$ u.c. increases M_S from $1.5 \mu_B$ /interfacial Mn for $M = 3$ to $2.8 - 2.9 \mu_B$ /interfacial Mn for $M = 6, 8$ (Figure 1a), where the reported moment was normalized by the number of interfacial Mn atoms at CRO/CMO interfaces. This evolution of Mn moment/interface contrasts starkly with the (001) SL value shown in Figure 1 as a dashed line. The large magnetization enhancement suggests that the emergent magnetization may not be confined to the interfacial Mn. Because the moment/interfacial Mn saturates at $M = 6$, we postulate that three layers of the CMO at the interface contribute to the magnetization.

1
2
3 This is supported by the lack of exchange bias in all samples, suggesting that an insuffi-
4 cient quantity of antiferromagnetically aligned CMO to enable pinning of the ferromagnetic
5 moment. Similar to (001)-oriented samples, the coercive field (H_C) slowly decreases with
6 increasing CMO thickness. Unlike (001)-oriented samples, we did not observe any even/odd
7 dependence on the magnetic moment nor any exchange bias of the magnetization loops.⁹
8
9

10
11 In a second series of SLs, CMO thickness was held constant at $M = 3$ u.c. while CRO
12 thickness was varied from $N = 3$ u.c. – 15 u.c.. The moment increased from $1.5 \mu_B$ /interfacial
13 Mn ion for $N = 3$ to $2.0 \mu_B$ /interfacial Mn for $N = 15$. While the total moment increase per
14 CRO unit cell was much smaller than for increasing CMO layer thickness, the net moment
15 continued to increase up to $N = 15$. A linear fit of these data points suggests that each ad-
16 ditional layer adds $0.05 \mu_B$ /Ru. This trend may indicate a small ferromagnetic contribution
17 from the CRO layers, which was not observed in (001)-oriented SLs.⁷
18
19

20
21 Temperature dependent magnetization measurements (Figure 1c) revealed an approx-
22 imately 175 K Curie temperature (T_C) for all samples, consistent with the onset of hys-
23 teretic magnetoresistance and an anomalous Hall effect in electrical transport measurements
24 (see Supplemental Material). This T_C is higher than the Néel temperature of bulk CMO
25 ($T_N = 123$ K)¹⁸ but within the 150 K – 210 K range observed for $\text{CaRu}_x\text{Mn}_{1-x}\text{O}_3$.^{19–22} How-
26 ever, if the increase in measured moment was due to changes in the degree of intermixing,
27 we would expect changes in T_C corresponding to trends in the measured moment. Instead,
28 T_C is independent of both CMO and CRO thickness, favoring a uniform interfacial origin.
29 A similar T_C enhancement observed in CMO/LaNiO₃ SLs from $T = 125$ K in (001)-oriented
30 SLs to $T = 200$ K in (111)-oriented SLs suggests that the Néel temperature of CMO depends
31 on growth direction.²³ In fact, past work on (Sr,Ca)MnO₃ and (Sr,Ba)MnO₃ shows that the
32 Néel temperature is enhanced by structural distortions which increase the Mn-O-Mn bond
33 angle and orbital overlap, with maximal values exceeding 230 K.²⁴ We speculate that (111)-
34 oriented strain and interface interactions play a similar role here, so that growth in the [111]
35 direction could serve as a powerful tool to enhance T_C of G-type antiferromagnets.
36
37
38
39
40
41
42
43
44
45
46
47
48
49
50
51
52
53
54
55
56
57
58
59
60

1
2
3 To understand the origins of the enhanced magnetization in CRO/CMO(111), we stud-
4 ied the evolution of the charge transfer from CRO to CMO as a function of layer thickness.
5 Specifically, we probed the chemical valence using electron energy loss spectroscopy (EELS)
6 and X-ray absorption spectroscopy (XAS). The EELS measurements were taken both at the
7 interface and the middle of the CMO layers (see Figure 2(a)) within a $[(\text{CMO})_3/(\text{CRO})_{15}]_5$
8 sample, at energies corresponding to the O K-edge and the Mn L-edge, shown in Figure 2(b)
9 and (c) respectively. Surprisingly, the Mn L_3 appears more intense relative to the L_2 near
10 the middle of the CMO layer, indicating lower Mn-valence and consequently higher charge
11 transfer near the CMO center. Such a finding is counterintuitive, and we propose that trans-
12 ferred electrons from both top and bottom interfaces may contribute to the signal near the
13 CMO center. Examining the L_3/L_2 separation and intensity ratio of the EELS measurements
14 yield valences of Mn^{3+} and $(\text{Mn}^{3.5+})$ at the center and interface, respectively. Recalling that
15 previously reported EELS measurements on (001)-oriented systems were consistent with a
16 valence shift of 0.1 (i.e. from Mn^{4+} to $\text{Mn}^{3.9+}$ at the interface,⁹ the enhancement of emer-
17 gent magnetism in (111)-oriented SLs is attributed to increased charge transfer relative to
18 the (001) orientation.

19
20 We confirmed these results with XAS and X-ray magnetic circular dichroism (XMCD) on a
21 $[(\text{CMO})_8/(\text{CRO})_6]_5$ SL (Figure 3), explicitly resolving the spectroscopic signatures of Mn^{2+} ,
22 Mn^{3+} , and Mn^{4+} . Based on the integrated L_3/L_2 intensity ratio, we estimated an average
23 valence of approximately $\text{Mn}^{3.2+}$, in excellent agreement with EELS. The Mn XMCD spectra
24 at $T = 73$ K (Fig. 3) explicitly identifies ferromagnetism on the Mn ions in these (111) SLs
25 whereas no XMCD signal was observed at 300K. Unfortunately, XMCD measurements at the
26 Ru edge were not possible due to the low x-ray interaction cross section of the Ru M-edge.
27 We must therefore use alternative methods, such as polarized neutron reflectometry (PNR),
28 to understand the contribution of Ru to the observed emergent magnetization.

29
30 PNR measurements were performed on a pair of $[(\text{CMO})_3/(\text{CRO})_N]_5$ SLs, where $N =$
31 12, 15, in order to separate the contributions of the CMO and CRO layers to the overall
32
33
34

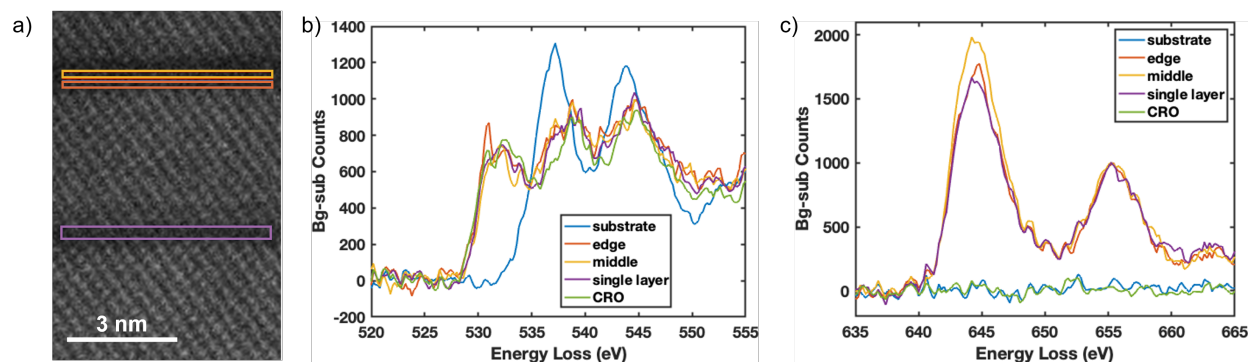


Figure 2: STEM-EELS measurements of a $[(\text{CMO})_3/(\text{CRO})_{15}]_5$ superlattice. a) STEM scan with colored boxes to indicate scan location, b) O K-edge measurements for various scans, c) Mn L-edge measurements for various scans.

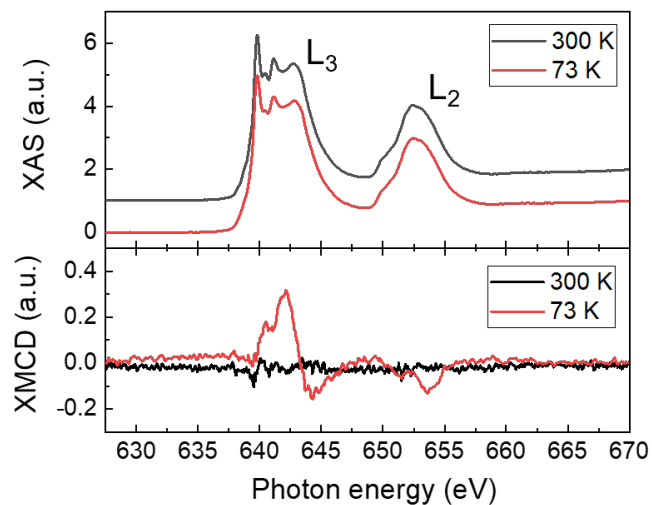


Figure 3: (top) Mn L-edge X-ray absorption and (bottom) x-ray magnetic circular dichroism measurements of a $[(\text{CMO})_8/(\text{CRO})_6]_5$ taken at 73 K and 300 K with $H = 0.7$ T.

1
2
3 magnetization of the samples. Both samples were fit simultaneously to a model with linked
4 parameters. For example, the nuclear (but not magnetic) SLDs of the CRO layers were
5 presumed to be uniform within each layer, between layers, and across both samples. Any
6 net CRO magnetization was confined to 3 u.c. layer at the interface. The CMO magnetic
7 SLD was allowed to vary between samples but was uniform and constant within each CMO
8 sublayer (see Supplemental Material for modeling details). Model optimization under these
9 constraints yields an excellent fit to the data, with reduced $\chi^2 = 1.35$. Interfacial roughness
10 parameters, which probe the combined effects of conformal roughness, intermixing, and thick-
11 ness variations, were approximately 0.8 nm, in excellent agreement with the XRR analysis.
12 The fitted spin-dependent reflectivities support the presence of a modulated ferromagnetic
13 moment concentrated in CMO layers, as shown in Figure 4. For the $N = 12$ sample, the
14 integrated magnetic SLD over all layers fit to the PNR data corresponded to $1.66 \mu_B \pm 0.1$
15 μ_B normalized per interfacial Mn ion (unless otherwise noted, uncertainties correspond to \pm
16 1 standard deviation). Similarly, fitting the $N = 15$ sample data yields a moment of $1.72 \mu_B$
17 $\pm 0.1 \mu_B$ per interfacial Mn ion. Both the extracted values and the thickness trend are in
18 good agreement with the values and trends shown in Figure 1. The increase in total moment
19 between the two samples with identical CMO layer thickness further supports the emergence
20 of ferromagnetism polarization in the CRO layers.

21
22
23
24
25
26
27
28
29
30
31
32
33
34
35
36
37
38
39 The PNR results support the stabilization of a magnetic polarization in the CRO layers.
40 The fitted CRO magnetization within 3 u.c. of the interface was $220(60)$ kA/m ($1.3(0.2)$
41 μ_B/Ru). Fitting the data with counterfactual models in which the CRO magnetization is ei-
42 ther constrained to be zero or uniformly distributed through the layer reduces the fit quality
43 to approximately 1.42. We therefore conclude that PNR favors a net magnetization origi-
44 nating in the CRO layers and localized near the interface. However, PNR cannot precisely
45 determine the thickness of the magnetized layer or the shape of the falloff away from the
46 interface. Additional details on PNR fitting and alternative models can be found in the
47 Supplemental Materials.
48
49
50
51
52
53
54
55
56
57
58
59
60

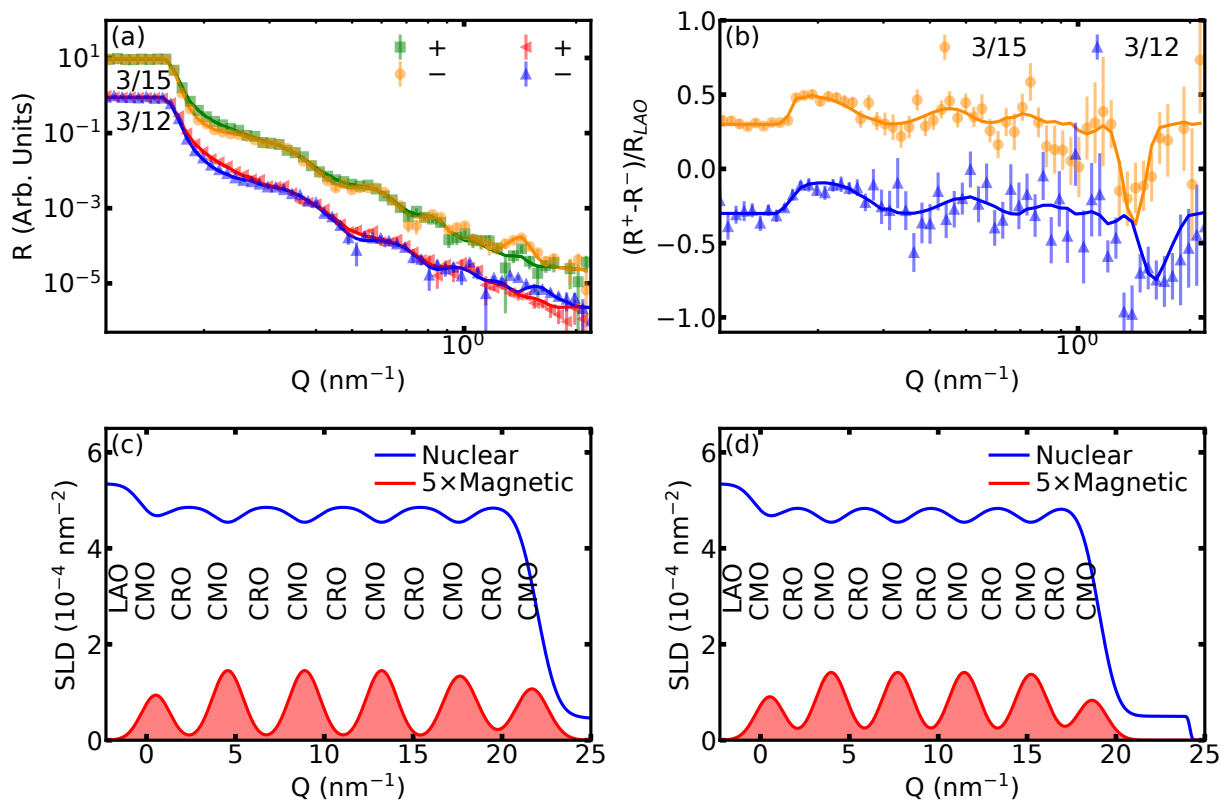


Figure 4: (a) Polarized neutron reflectometry measurements performed on (111)-oriented $[(\text{CMO})_3/(\text{CRO})_{15}]_5$ and $(\text{CMO})_3/(\text{CRO})_{12}]_5$ samples alongside theoretical fits. (b) Fresnel-normalized spin difference associated with the same samples, alongside the same theoretical curves. (c) Best-fit nuclear and magnetic SLD profiles for the 3/15 SL (d) Best-fit nuclear and magnetic SLD profiles for the 3/12 SL. Error bars represent ± 1 standard deviation.

To place our experimental results into theoretical context, we performed density-functional theory (DFT) calculations on three superlattice geometries: (1) three layers of CMO and six layers of CRO (3CMO/6CRO), (2) three layers of CMO and twelve layers of CRO (3CMO/12CRO), and (3) six layers of CMO and six layers of CRO (6CMO/6CRO) along the body diagonal [111] direction of the pseudocubic perovskite unit cell. We constrained the in-plane lattice constant to match the substrate $\text{LaAlO}_3(111)$ and preserved the experimental volume of each unit cell, then optimized the atomic positions with force less than 10^{-3} eV/Å.

Two solutions with similar energies were obtained for odd layers of CMO and are shown schematically in Fig. 5. Both solutions have a robust, antiferromagnetically-aligned MnO layers, but differ in the magnetic moments of the Ru atoms in the CRO layers. The first solution (type I) includes a significant magnetic moment induced on Ru ions in proximity to the interface with CMO. The second solution (type II) exhibits no magnetic moment in the ruthenium. While the two solutions have similar net moment, the type I solution is lower energy (see Table 1), implying that ferromagnetism is likely to be induced in the CRO layers. In all superlattice models, the Ru moment decreases quickly away from the CMO/CRO interface. Values are presented in Table 1 and a partial densities of states for each atom are shown in Figure S4 in the Supplementary Section.

Table 1: Magnetic moments of Mn and Ru (units of μ_B) in the $M\text{CMO}/N\text{CRO}$ superlattices, with $(M, N) = (3, 6)$ or $(3, 12)$. The net magnetization of the entire superlattice is indicated by μ_{tot} , and the total energy (in eV) is with respect to the type II structure. The subscripts on the atoms, $i = 1 \cdots M$ or N , denote the individual layers as indicated in Fig. 5. The paired indices indicate symmetry-equivalent atoms.

$M\text{CMO}/N\text{CRO}$	Mn _{1,3} , Mn ₂	Ru _{1,6} , Ru _{2,5} , Ru _{3,4}	μ_{tot}	Energy
(3,6) Type I	-2.68, 2.33	1.22, 1.07, 0.05	3.81	-0.09
(3,6) Type II	-2.66, 2.43	-0.02, -0.10, 0.00	-3.58	0.00
(3,12) Type I	-2.68, 2.35	Ru _{1,12} , Ru _{2,11} , Ru _{3,10} , Ru _{4,9} , Ru _{5,8} , Ru _{6,7} 1.15, 1.09, 0.03, 0.00, -0.04, 0.08	3.84	-0.20
(3,12) Type II	-2.64, 2.34	-0.01, -0.14, 0.11, -0.05, 0.01, 0.03	-3.60	0.00

For both geometries with three CMO layers, CMO maintains G-type antiferromagnetic

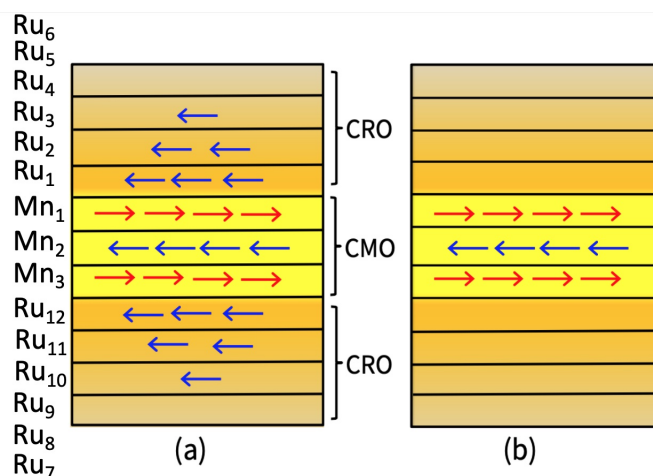


Figure 5: Schematic diagram showing spin polarized electron gas in *MCMO/NCRO* ($M = 3$ and $N = 12$) [111] superlattice in (a) type I and (b) type II solutions. As indicated from the figures, the spin polarization quickly becomes zero as one moves away from the interface.

ordering, but the moment on Mn sites in adjacent (111) layers are not equal. The middle layer Mn has a moment $0.34 \mu_B$ smaller than the interfacial layers, yielding a net moment of about $1.9 \mu_B$ per interface. In the 6CMO/6CRO case, the structure is not symmetric, and we consequently find a non-symmetric solution in the magnetic moment. We find that the two Mn layers adjacent to one of the interfaces are ferromagnetically coupled, while the remaining layers are anti-aligned, with the total moment per interface increasing to $2.3 \mu_B$. Thus, predictions in all cases match the experimentally observed increase in interfacial moments relative to the (001) orientation. Note that this model does not include considerations for Mn-moment canting, as would be expected from itinerant electron exchange. For the (111) interface, the Mn 3d states are much more delocalized (see Fig. S4 layer resolved partial density of states) in contrast to the CMO/CRO(001) interface.²⁵ We find that all three CMO layers acquire a similar number of itinerant electrons leaked from the CRO side, ≈ 0.09 and ≈ 0.06 electrons for 3CMO/6CRO and 3CMO/12CRO, respectively. In the 6CMO/6CRO SL, the average charge acquired by interfacial Mn is 0.093 electrons, while the middle Mn layers acquire ≈ 0.06 electrons per Mn. The charge transfer decreases away from the interface, but it is not obvious how far the itinerant electrons leak in the CMO layers.

We now combine all of our observations into a complete picture of the magnetic ground

1
2
3 state in (111)-oriented CRO/CMO superlattices. SQUID magnetometry and PNR confirm
4 enhanced emergent magnetization, while EELS and XAS demonstrate a larger shift in Mn-
5 valence relative to (001)-oriented samples. Evidence of different Mn-valences in the center
6 and interfacial CMO, coupled with XAS lineshapes supporting Mn²⁺, Mn³⁺, and Mn⁴⁺ pro-
7 vide hints of a new charge-disproportionated ground state induced by enhanced electron
8 transfer. A more detailed thickness-dependent STEM/EELS study of the thickness depen-
9 dent structure and valence would shed light on this question. The shift in Mn valence is
10 unlikely to originate from Mn-Ru intermixing, as CRO/CMO alloys do not exhibit valences
11 below Mn^{3.6+}.²⁶ Further, is no evidence of greater interfacial alloying with increasing thick-
12 ness, since the CRO/CMO interfacial roughness measured through AFM, XRR, and PNR
13 is similar across all SLs. Further, T_C in an alloy would be expected to vary with the degree
14 of intermixing, but is instead independent of layer thickness while the net moment doubles.
15 Rather, we suggest that the increased charge transfer is due to the strain state at the (111)
16 interface, where increased interfacial connection between CRO and CMO constrain octahe-
17 dral tilting as compared to the (001) interface. This increased charge transfer at the (111)
18 interfaces enhances the emergent ferromagnetism. PNR, magnetometry and DFT calcula-
19 tions all suggest a contribution to the emergent ferromagnetism from a weak magnetization
20 of the Ru, with some ambiguity regarding the spatial extent of this induced moment. Theory
21 and PNR favor a rapid decay away of induced CRO moment from the interface with CMO
22 while magnetometry reveals an increase in magnetization with CRO thickness which persists
23 up to 15 CRO unit cells.
24
25
26
27
28
29
30
31
32
33
34
35
36
37
38
39
40
41
42
43
44

45 In this work, we have demonstrated massive enhancement of the emergent interfacial
46 magnetization and ordering temperature in CRO/CMO superlattices through interfacial
47 symmetry modification. By growing the superlattices on (111)-oriented substrates rather
48 than (001) , the net magnetization is enhanced by nearly a factor or three. Through com-
49 prehensive multimodal characterization and calculations, we can attribute this enhancement
50 not to increased intermixing but rather modifications in the interface symmetry which alters
51
52
53
54
55
56
57
58
59
60

1
2
3 octahedral connectivity and hence exchange interactions. These results illustrate the power
4 of interface symmetry in controlling the magnetic ground state in quantum materials and
5 correlated electron systems, opening a new pathway for stabilizing novel phases of matter.
6
7
8
9

10 11 **Acknowledgement**

12
13
14 The research was supported by the US Department of Energy, Director, Office of Science, Of-
15 fice of Basic Energy Sciences, Division of Materials Sciences and Engineering under Contract
16 No. DESC0008505. A portion of this research used resources at the MAGREF beamline at
17 the Spallation Neutron Source, a DOE Office of Science User Facility operated by the Oak
18 Ridge National Laboratory. Part of this work was performed at the Stanford Nano Shared
19 Facilities (SNSF), supported by the National Science Foundation under award no. EECS-
20 1542152. This material is based upon work supported by the National Science Foundation
21 Graduate Research Fellowship grant number DGE-1656518. Certain commercial equipment,
22 instruments, software, or materials are identified in this paper in order to specify the exper-
23 imental procedure adequately. Such identifications are not intended to imply recommenda-
24 tion or endorsement by NIST, nor it is intended to imply that the materials or equipment
25 identified are necessarily the best available for the purpose. Theoretical and computational
26 research was conducted at Ames National Laboratory for the U.S. DOE with Iowa State
27 University under Contract No. DE-AC02-07CH11358. Work at National Yang Ming Chiao
28 Tung University was supported by NSTC 112-2112-M-A49-026.
29
30
31
32
33
34
35
36
37
38
39
40
41
42
43
44
45
46

47 **Supporting Information Available**

48
49
50 Supplementary Materials describe (i) methods of sample synthesis, structural, chemical,
51 magnetic and transport characterization as well as additional results on (ii) x-ray reflectivity,
52 (ii) scanning transmission electron microscopy imaging, (iii) polarized neutron reflectivity,
53 (iv) electrical transport and (v) theoretical calculations. They can be found at:
54
55
56
57
58
59
60

References

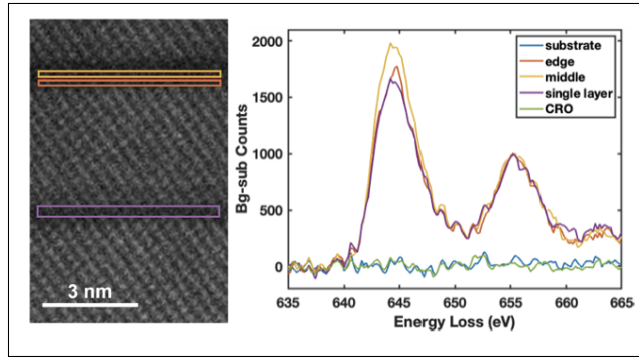
- (1) Gong, C.; Li, L.; Li, Z.; Ji, H.; Stern, A.; Xia, Y.; Cao, T.; Bao, W.; Wang, C.; Wang, Y.; Qiu, Z. Q.; Cava, R. J.; Louie, S. G.; Xia, J.; Zhang, X. Discovery of intrinsic ferromagnetism in two-dimensional van der Waals crystals. *Nature* **2017**, *546*, 265–269.
- (2) Huang, B.; Clark, G.; Navarro-Moratalla, E.; Klein, D. R.; Cheng, R.; Seyler, K. L.; Zhong, D.; Schmidgall, E.; McGuire, M. A.; Cobden, D. H.; Yao, W.; Xiao, D.; Jarillo-Herrero, P.; Xu, X. Layer-dependent ferromagnetism in a van der Waals crystal down to the monolayer limit. *Nature* **2017**, *546*, 270–273.
- (3) Huang, B.; Clark, G.; Klein, D. R.; MacNeill, D.; Navarro-Moratalla, E.; Seyler, K. L.; Wilson, N.; McGuire, M. A.; Cobden, D. H.; Xiao, D.; Yao, W.; Jarillo-Herrero, P.; Xu, X. Electrical control of 2D magnetism in bilayer CrI₃. *Nature Nanotechnology* **2018**, *13*, 544–548.
- (4) Jiang, S.; Li, L.; Wang, Z.; Mak, K. F.; Shan, J. Controlling magnetism in 2D CrI₃ by electrostatic doping. *Nature Nanotechnology* **2018**, *13*, 549–553.
- (5) Boschker, H. et al. Ferromagnetism and Conductivity in Atomically Thin SrRuO₃. *Phys. Rev. X* **2019**, *9*, 011027.
- (6) Cui, Z. et al. Correlation-driven eightfold magnetic anisotropy in a two-dimensional oxide monolayer. *Science Advances* **2020**, *6*, eaay0114.
- (7) Takahashi, K. S.; Kawasaki, M.; Tokura, Y. Interface ferromagnetism in oxide superlattices of CaMnO₃/CaRuO₃. *Applied Physics Letters* **2001**, *79*, 1324–1326.
- (8) Freeland, J. W.; Chakhalian, J.; Boris, A. V.; Tonnerre, J.-M.; Kavich, J. J.; Yordanov, P.; Grenier, S.; Zschack, P.; Karapetrova, E.; Popovich, P.; et al. Charge trans-

- port and magnetization profile at the interface between the correlated metal CaRuO_3 and the antiferromagnetic insulator CaMnO_3 . *Physical Review B* **2010**, 094414.
- (9) He, C.; Grutter, A. J.; Gu, M.; Browning, N. D.; Takamura, Y.; Kirby, B. J.; Borchers, J. A.; Kim, J. W.; Fitzsimmons, M. R.; Zhai, X.; et al. Interfacial Ferromagnetism and Exchange Bias in $\text{CaRuO}_3/\text{CaMnO}_3$ Superlattices. *Physical Review Letters* **2012**, *109*, 197202.
- (10) Grutter, A. J.; Vailionis, A.; Borchers, J. A.; Kirby, B. J.; Flint, C. L.; He, C.; Arenholz, E.; Suzuki, Y. Interfacial Symmetry Control of Emergent Ferromagnetism at the Nanoscale. *Nano Letters* **2016**, *16*, 5647–5651.
- (11) Grutter, A.; Kirby, B.; Gray, M.; Flint, C.; Alaun, U.; Suzuki, Y.; Borchers, J. Electric Field Control of Interfacial Ferromagnetism in $\text{CaMnO}_3/\text{CaRuO}_3$ Heterostructures. *Physical Review Letters* **2015**, *115*, 047601.
- (12) Nanda, B. R. K.; Satpathy, S.; Springborg, M. S. Electron Leakage and Double-Exchange Ferromagnetism at the Interface between a Metal and an Antiferromagnetic Insulator: $\text{CaRuO}_3/\text{CaMnO}_3$. *Physical Review Letters* **2007**, *98*, 216804.
- (13) He, C.; Zhai, X.; Mehta, V. V.; Wong, F. J.; Suzuki, Y. Interfacial magnetism in $\text{CaRuO}_3/\text{CaMnO}_3$ superlattices grown on (001) SrTiO_3 . *Journal of Applied Physics* **2011**, *109*, 07D729.
- (14) Flint, C. L.; Vailionis, A.; Zhou, H.; Jang, H.; Lee, J.-S.; Suzuki, Y. Tuning interfacial ferromagnetism in $\text{LaNiO}_3/\text{CaMnO}_3$ superlattices by stabilizing nonequilibrium crystal symmetry. *Phys. Rev. B* **2017**, *96*, 144438.
- (15) Hallsteinsen, I.; Moreau, M.; Grutter, A.; Nord, M.; Vullum, P.-E.; Gilbert, D. A.; Bolstad, T.; Grepstad, J.; Holmestad, R.; Selbach, S.; others Concurrent magnetic and structural reconstructions at the interface of (111)-oriented $\text{La}_{0.7}\text{Sr}_{0.3}\text{MnO}_3/\text{LaFeO}_3$. *Physical Review B* **2016**, *94*, 201115.

- 1
2
3 (16) Hallsteinsen, I.; Grutter, A.; Moreau, M.; Slöetjes, S. D.; Kjærnes, K.; Arenholz, E.;
4 Tybell, T. Role of antiferromagnetic spin axis on magnetic reconstructions at the (111)-
5 oriented $\text{La}_{0.7}\text{Sr}_{0.3}\text{MnO}_3/\text{LaFeO}_3$ interface. *Physical Review Materials* **2018**, *2*, 084403.
6
7
8
9
10 (17) Caspi, E. N.; Avdeev, M.; Short, S.; Jorgensen, J. D.; Lobanov, M. V.; Zeng, Z.;
11 Greenblatt, M.; Thiyagarajan, P.; Botez, C. E.; Stephens, P. W. Structural and mag-
12 netic phase diagram of the two-electron-doped $(\text{Ca}_{1-x}\text{Ce}_x)\text{MnO}_3$ system: Effects of
13 competition among charge, orbital, and spin ordering. *Phys. Rev. B* **2004**, *69*, 104402.
14
15
16
17
18 (18) Wollan, E. O.; Koehler, W. C. Neutron Diffraction Study of the Magnetic Properties
19 of the Series of Perovskite-Type Compounds $[(1-x)\text{La}, x\text{Ca}]\text{MnO}_3$. *Physical Review*
20 **1955**, *100*, 545–563.
21
22
23
24
25 (19) He, T.; Cava, R. J. The effect of Ru-site dopants on the magnetic properties of CaRuO_3 .
26 *Journal of Physics: Condensed Matter* **2001**, *13*, 8347–8361.
27
28
29
30 (20) Maignan, A.; Martin, C.; Hervieu, M.; Raveau, B. Ferromagnetism and metallicity in
31 the $\text{CaMn}_{1-x}\text{Ru}_x\text{O}_3$ perovskites: a highly inhomogeneous system. *Solid state commu-*
32 *nications* **2001**, *117*, 377–382.
33
34
35
36
37 (21) Mizusaki, S.; Taniguchi, T.; Okada, N.; Nagata, Y.; Hiraoka, N.; Itou, M.; Sakurai, Y.;
38 Noro, Y.; Ozawa, T. C.; Samata, H. Magnetic ground states of $\text{CaRu}_{1-x}\text{Mn}_x\text{O}_3$ (0.2
39 $\leq x \leq 0.9$): a magnetic Compton scattering study. *Journal of Physics: Condensed*
40 *Matter* **2009**, *21*, 276003.
41
42
43
44
45 (22) Kawanaka, H.; Yokoyama, M.; Noguchi, A.; Bando, H.; Nishihara, Y. Itinerant electron
46 magnetism in $\text{CaRu}_{1-x}\text{Mn}_x\text{O}_3$ ($0 \leq x \leq 0.5$). *Journal of Physics: Condensed Matter*
47 **2009**, *21*, 296002.
48
49
50
51
52 (23) Flint, C. L.; Yi, D.; Karapetrova, E.; N'Diaye, A. T.; Shafer, P.; Arenholz, E.;
53 Suzuki, Y. Enhanced interfacial ferromagnetism and exchange bias in (111)-oriented
54 $\text{LaNiO}_3/\text{CaMnO}_3$ superlattices. *Physical Review Materials* **2019**, *3*, 064401.
55
56
57
58
59
60

- 1
2
3 (24) Chmaissem, O.; Dabrowski, B.; Kolesnik, S.; Mais, J.; Brown, D. E.; Kruk, R.; Prior, P.;
4 Pyles, B.; Jorgensen, J. D. Relationship between structural parameters and the Néel
5 temperature in $\text{Sr}_{1-x}\text{Ca}_x\text{MnO}_3$ ($0 \lesssim x \lesssim 1$) and $\text{Sr}_{1-y}\text{Ba}_y\text{MnO}_3$ ($y \lesssim 0.2$). *Physical*
6 *Review B* **2001**, *64*, 134412.
7
8
9
10
11
12 (25) Bhandari, C.; Satpathy, S. Dielectric screening and electric field control of ferromag-
13 netism at the $\text{CaMnO}_3/\text{CaRuO}_3$ interface. *Physical Review B* **2021**, *104*, 085134.
14
15
16
17 (26) Zhou, Q.; Kennedy, B. J.; Zhang, Z.; Jang, L.-Y.; Aitken, J. B. X-ray Absorption near
18 Edge Structure and Crystallographic Studies of the Mixed Valence Oxides CaRu_{1-x}
19 Mn_xO_3 . *Chemistry of Materials* **2009**, *21*, 4203–4209.
20
21
22
23
24
25
26
27
28
29
30
31
32
33
34
35
36
37
38
39
40
41
42
43
44
45
46
47
48
49
50
51
52
53
54
55
56
57
58
59
60

TOC Graphic



1
2
3
4
5
6
7
8
9
10
11
12
13
14
15
16
17
18
19
20
21
22
23
24
25
26
27
28
29
30
31
32
33
34
35
36
37
38
39
40
41
42
43
44
45
46
47
48
49
50
51
52
53
54
55
56
57
58
59
60